Ultrasonics 99 (2019) 105965

Contents lists available at ScienceDirect

Ultrasonics

journal homepage: www.elsevier.com/locate/ultras

A new beamforming method and hardware architecture for real time two way dynamic depth focusing

Jorge F. Cruza[a,*], Jorge Camacho[b], Raúl Mateos[c], Carlos Fritsch[b]

[a] DASEL, Avda. del Cañal 44 Nave 3, 28500 Arganda del Rey, Madrid, Spain
[b] Ultrasound Systems and Technology Group (GSTU), Spanish National Research Council (CSIC), c/ Serrano 144, 28006 Madrid, Spain
[c] Department of Electronics, University of Alcalá de Henares (UAH), Edificio Politécnico, Campus Universitario, Alcalá de Henares, Spain

ARTICLE INFO

Keywords:
Total Focus Phased Array
Virtual array
Dynamic Depth Focusing
DDF
Dynamic Depth Full Focusing
DDFF
Beamforming
Refraction

ABSTRACT

The Total Focusing Method (TFM) yields a focused image in emission and in reception while Phased Array (PA) imaging provides Dynamic Depth Focusing (DDF) in reception only. Besides, most NDE applications have two propagation media, where refraction at the interface complicates time-of-flight (TOF) and focal law computations. This affects especially TFM, which must compute the TOFs from all elements to image pixels and use them to select the data for imaging.

A new method with real-time Dynamic Depth Full Focusing (DDFF), in emission and reception, is proposed in this work. It is called Total Focusing Phased Array (TFPA) because it uses concepts of TFM and PA. Omnidirectional emissions are used to create a synthetic aperture as in TFM, while beamforming is carried out along scan lines as in PA, simplifying the delay calculation in the presence of interfaces and providing an efficient hardware implementation.

Refraction at the interface between two media is eliminated by a Virtual Array (VA) that converts such scenario into a simple homogeneous medium. Propagation can be considered along scan lines from the virtual array at constant speed, as in homogeneous media. Strict dynamic focusing is performed in real-time, an important difference with other approaches that require iterative Fermat search to get the focal laws for every imaged point. With TFPA only 3 parameters per element and scan line are required to perform this task.

Experiments are carried out to compare the three techniques, PA, TFM and TFPA. TFM and TFPA yield similar image quality, offering improved depth of field and resolution over PA. On the other hand, TFPA avoids most of the burden for computing TOFs and operates in real time with one or two media propagation.

1. Introduction

Synthetic aperture techniques have been used in ultrasound imaging for more than four decades with different strategies. In the monostatic or Synthetic Aperture Focusing Technique (SAFT) every array element emits an omnidirectional wave and acquires the A-scan. Virtual sources created with focused subapertures have been also used to increase the emitted energy [1,2]. In any case, the image is formed from the coherent addition of the acquired data that correspond to the same pixel position [3,4].

The Synthetic Transmit Aperture (STA) is an extension of SAFT, where the emitting aperture is synthesized changing the emitter position. Following every emission, the whole N-element aperture is used for reception [5,6]. The contributing samples to every pixel are coherently added considering the Time-Of-Flight (TOF) emitter-pixel-receiver, forming a low-resolution image. The process is repeated for all possible emitter positions and the final high-resolution image, focused in emission and reception, is obtained by averaging the N single emitter images.

The more recent application of STA to Non Destructive Evaluation (NDE) has been renamed Total Focusing Method (TFM) [7] or even Sampling Phased Array (SPA) [8], both sharing the same principles of STA. As the TFM term has prevailed, it will be used in this work. The complete data set of $N \times N$ A-scans acquired by the N-element array after N consecutive triggers is called Full Matrix Capture (FMC), from which data are post-processed by coherent addition as in the precedent cases [9,10].

TFM images are focused in emission and in reception, because the beamforming process takes into account the emitter–pixel–receiver TOFs. By contrast, phased array (PA) imaging provides strict dynamic

---

* Corresponding author.
E-mail address: cruza@daselsistemas.com (J.F. Cruza).

https://doi.org/10.1016/j.ultras.2019.105965
Received 16 October 2018; Received in revised form 5 July 2019; Accepted 19 July 2019

focusing (all samples focused) only in reception. TFM has also the ability of imaging beyond the array projection [11] and of combining different propagation modes from the same data set [12].

On the other hand, performing TFM in the time domain involves a computing intensive process: for two propagation media, it must estimate the TOFs from each array element to every image pixel by numerical methods. The wavenumber algorithm produces the image in the Fourier domain with less computational demands [13]. Other time-domain approaches use multi-CPU/GPU platforms that benefit from the parallelization possibilities of TFM [14], but frame rate and image size are usually limited by communications and memory bandwidth restrictions. Also, a real-time FPGA implementation has been reported and commercial equipment is available for moderate size images and number of array elements [15].

TFM has also some other limitations, one of them being the lack of a physical beam, a problem to comply with some requirements of NDE standards. Besides, single element emission has low energy, which reduces the SNR. By contrast, the conventional PA technology uses focused beams in emission with higher energy and programmable steering angles. PA provides A-scans in real-time with simple delay and sum beamformers [16,17]. Another advantage of A-scan beamforming is the availability of circuits to compute the focusing delays in real-time for homogeneous media [18,19]. Such hardware performs strict Dynamic Depth Focusing (DDF) in reception.

However, the main problems for TFM and PA in NDE arise in two-media scenarios as, for example, in immersion inspections. While in homogeneous media TOFs are the ratio of distances to sound propagation velocity, refraction at the interface introduces complications. It is usually considered that the sound follows the fastest path (Fermat's principle), which must be found by iterative procedures and approximate methods [20].

The Fast Focal Law Computing method (FFLC) used a Newton-Raphson algorithm without iterations due to the proximity between samples in PA imaging [21]. Its application to TFM requires several iterations to keep low timing errors, but adapting the focal laws to geometric changes in real-time is possible for limited size images [22]. Due to the computing burden, TOFs for TFM are frequently computed off line and stored to be used during the inspection process [23].

This work proposes the Total Focus Phased Array technique (TFPA), which tries to keep the best of both worlds, PA and TFM: real-time strict focusing in emission and reception, sector or linear scan images and no refraction issues at the interface between propagating media. These results have been obtained with three key achievements: virtual arrays that avoid the complications of refraction, real-time strict focusing hardware and a parallel architecture performing at high speed.

The virtual array concept for TFPA is addressed in Section 2 as an extension of the original proposal for PA. Section 3 presents the real-time focusing hardware and the TFPA beamforming process. Finally, Section 4 describes validation experiments that compare the performances of PA, TFM and TFPA.

2. The virtual array concept for TFPA

TFPA beamforming is carried out along scan lines, as in PA, but with focusing in emission and reception at all depths or Dynamic Depth Full Focusing (DDFF). Beamforming along scan lines instead of at image pixels enables an accurate delay calculation based on only two Fermat searches per line, and the resulting implementation can be made very efficient.

However, refraction introduces complications. Refraction changes the direction of the ultrasonic beam at the interface entry point following the Snell's law. The equivalent Fermat's principle (the shortest TOFs from the emitter or receiver element to the image pixel crossing the interface) defines the entry point coordinates. These are found by approximate iterative procedures due to the lack of closed formulae. In TFM, the process has to be applied to all pairs (array elements, image pixels) with an important computing burden, but is the only method available until now.

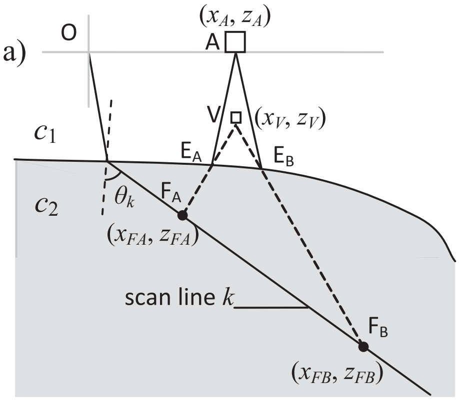

Fig. 1. Geometry used in PA to find the virtual element V coordinates.

By contrast, TOFs for arrays operating in homogeneous media are directly obtained as the ratio of distance to sound velocity, without iterative procedures. The idea behind the *virtual array* concept is to convert a two-media propagation scenario into a single, homogeneous medium, without refraction. The virtual array provides TOFs that approximate those of the real array to foci located in a ray inside the second medium. This was first proposed by our group to overcome refraction issues for PA imaging [24,25]. Besides, strict DDF was achieved in real time by a simple focusing digital circuit. This avoided computing the set of focal laws through the interface along the propagation path.

2.1. Virtual array principle

A short background on the virtual array concept is given here, highlighting the specific points involved in TFPA. Differently from the initial idea (DDF in reception), virtual arrays are applied to get dynamic focusing in both, emission and reception, or DDFF.

Fig. 1 shows the geometry to compute the coordinates (x_V, z_V) of the virtual element V that corresponds to the array element A at (x_A, z_A) for focusing along scan line k. Sound propagation velocities are c_1 and c_2 for the coupling medium and the part, respectively.

Ideally, the TOF from element A to some focus F with refraction at the interface should equal that from V to F in a straight path at propagation velocity c_2, plus a constant t_k for A-scan k. This is forced at two points in the ray path F_A (x_{FA}, z_{FA}) and F_B (x_{FB}, z_{FB}), with TOFs t_A and t_B from A, respectively. For virtual element coordinates (x_V, z_V),

$$\frac{\sqrt{(x_V - x_{FA})^2 + (z_V - z_{FA})^2}}{c_2} + t_k = t_A$$
$$\frac{\sqrt{(x_V - x_{FB})^2 + (z_V - z_{FB})^2}}{c_2} + t_k = t_B \qquad (1)$$

Calling t_{AB} to the TOF from A to entry point E_B, it is found [24]:

$$t_k = t_{AB}(1 - c_1^2/c_2^2). \qquad (2)$$

Since (x_V, z_V) are solutions of (1), the TOFs from V to F_A and F_B are exact (equal to t_A and t_B) and *approximately equal* to nearby foci.

On the other hand t_A and t_B are obtained searching for the shortest TOF from each array element A to F_A and F_B (Fermat's principle). This process finds simultaneously the coordinates of the entry points E_A and E_B and, hence, the value t_{AB} required by (2).

Thus, although there are not closed formulae, the search is applied just 2 times per scan line instead of to all pairs of array elements and image pixels. Furthermore, the result can be obtained by hardware in real-time [26].

In TFPA a virtual array is computed for every scan line, shared in emission and reception (Fig. 2). E and R represent emitter and receiver

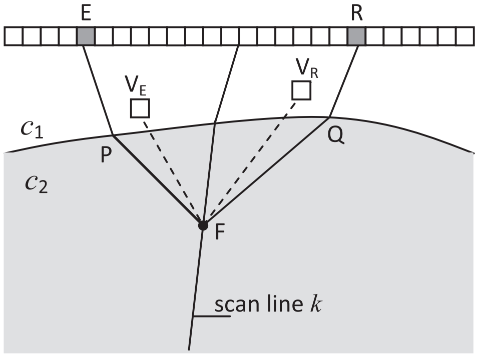

Fig. 2. Extension to consider the TOFs to focus F from emitter (E) and to receiving (R) elements and the corresponding virtual elements V_E and V_R, computed as in PA for the scan line k.

elements, while V_E and V_R are their virtual array counterparts, whose coordinates are computed as before.

Ultrasound refracts at the interface between the two media with propagation velocities c_1 and c_2. For TFM, the two-way TOF to some point F is:

$$TOF_{TFM} = \frac{EP}{c_1} + \frac{PF}{c_2} + \frac{FQ}{c_2} + \frac{QR}{c_1} \tag{3}$$

where the unknown coordinates of points P and Q must be found by Fermat search.

By contrast, propagation from the corresponding virtual elements V_E and V_R follows straight paths at constant velocity c_2, without refraction. The two-way time-of-flight for TFPA is the sum of the emitter-to-sample and the sample-to-receiver partial TOFs, each one computed by its own virtual array, resulting:

$$TOF_{TFPA} = \frac{V_E F + V_R F}{c_2} + t'_k \tag{4}$$

where t'_k is the constant for every A-scan line that results from the addition of the t_k values of the emitter and receiver virtual arrays for scan line k.

Beamforming either with TOF_{TFM} or TOF_{TFPA} produces images focused in emission and in reception. A single virtual array provides enough timing precision for PA in a wide range around the reference foci F_A and F_B. The small TOF errors had no or barely noticeable effects on the image [24]. Here, the timing errors of TOF_{TFPA} provided by (4) are the absolute difference with the TOF emitter-focus-receiver computed with the conventional Fermat technique with refraction at the interface.

2.2. TFPA timing errors

A general closed expression for timing errors at points other than F_A and F_B is not possible. However, to gain some insight in this subject, a typical case is considered: imaging in water immersion (c_1 = 1480 m/s) a plane part (c_2 = 6200 m/s) at $z = 0$ with an array parallel at z = 30 mm, N = 64-elements and d = 0.65 mm pitch. TOF from some element at (x_A, z_A) to a focus at (x_F, z_F) through the unknown entry-point $(x_E, 0)$ in the interface is:

$$TOF = \frac{\sqrt{(x_E - x_A)^2 + z_A^2}}{c_1} + \frac{\sqrt{(x_E - x_F)^2 + z_F^2}}{c_2} \tag{5}$$

Following the Fermat principle, the TOF is minimum and, thus, its derivative is zero:

$$f(x) = \frac{x - x_A}{c_1\sqrt{(x - x_A)^2 + z_A^2}} + \frac{x - x_F}{c_2\sqrt{(x - x_F)^2 + z_F^2}} = 0 \tag{6}$$

The Newton-Raphson method was used to solve Eq. (6) by successive approximations until the residual error was below 10^{-6} m, giving the entry-point coordinates $(x_E, z_E) = (x, 0)$. Then (5) is used to obtain TOF_{TFM} for comparisons.

Virtual arrays for steering angles θ = 10° and θ = 50° were computed from (1) and (2), with reference focus F_A and F_B set at 10% and 60% of the 0–100 mm range within the part, respectively. For every range, the TOF error is computed as,

$$\varepsilon = TOF_{TFPA} - TOF_{TFM} \tag{7}$$

Fig. 3a shows these errors as a function of range R, with element #1 as the emitter, all array elements as receivers and steering angle θ = 10°. Fig. 3b shows these errors when the emitter is element #32 and θ = 50°. The small boxes show the array (gray), the virtual array (black) and points F_A and F_B.

In both cases timing errors are zero at F_A and F_B and relatively small at other ranges, as expected. Higher errors are found near the interface ($R \approx 0$), which makes it advisable to use dynamic aperture in this region.

The effect of dynamic aperture at lower ranges can be seen in Fig. 4, which shows the rms timing error (*RMSE*) of the whole array as a function of *R*. If no dynamic aperture is used, the *RMSE* is higher than 100 ns for R < 5 mm (Fig. 4a). Dynamic aperture linearly applied until this range reduces errors to below 25 ns (Fig. 4b). To further reduce this error, the location of F_A should be moved towards the array, looking for a trade-off between error values before and after F_A position.

Fig. 5 compares the simulated lateral profile at R = 24 mm and θ = 10° for the Fermat-based TOF calculations (TFM) and for the virtual

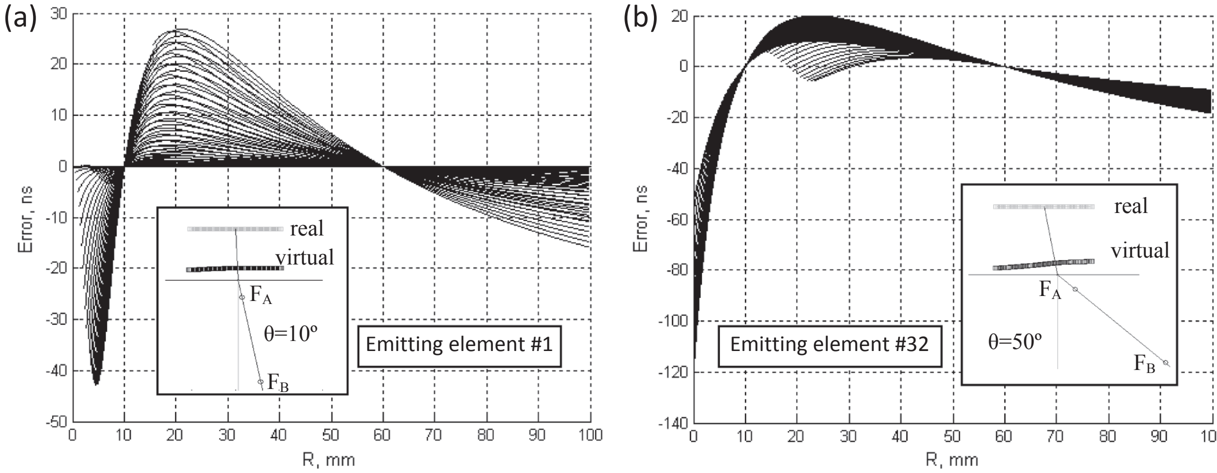

Fig. 3. Differences in the TOFs obtained with virtual arrays and those found by Fermat with refraction: (a) Emitting with element 1 and θ = 10°; (b) Emitting with element 32 and θ = 50°.

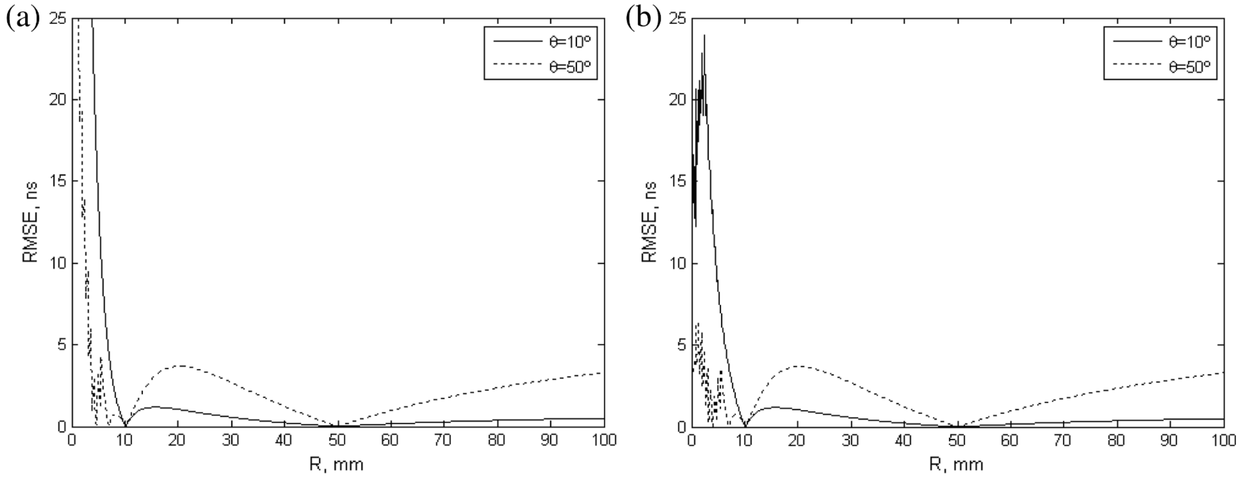

Fig. 4. TFPA rms timing errors for $\theta = 10^\circ$ and 50°: (a) without dynamic aperture (rmse > 100 ns); (b) applying dynamic aperture in reception only.

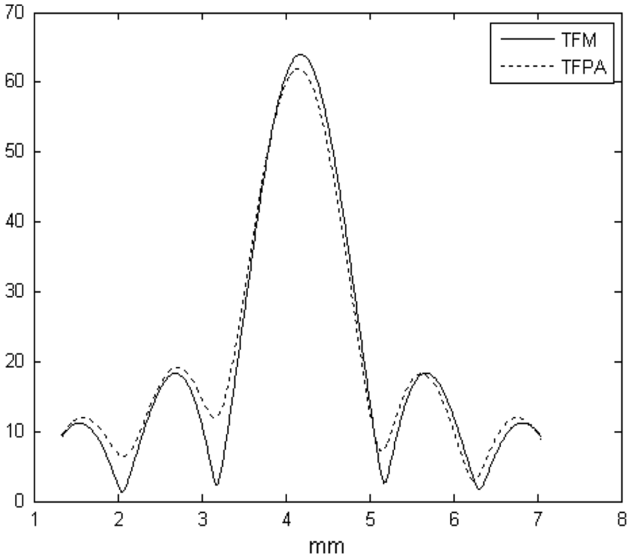

Fig. 5. Continuous wave lateral profile of TFM and TFPA at $R = 24$ mm and $\theta = 10^\circ$ when emitting with element 1, where timing errors are higher.

array (TFPA), when emitting with element 1. Virtual array timing errors produce slight losses in amplitude (3%) and resolution (beamwidth changes from 1.24 to 1.25 mm), as well as some increase in the sidelobe level. Higher sidelobe level and lower main lobe amplitude reduce the image dynamic range. An estimation of the relative sidelobe level increase η is given in [27] as:

$$\eta \approx \frac{\pi}{\mu\sqrt{6N}} \quad \mu >> 1 \tag{8}$$

where μ is the relation of the received signal period to the delay time errors. For a 64-element, 5 MHz array and a TOF rms error of 40 ns, application of (8) yields $\mu = 5$ and an expected dynamic range reduction of about 3.2%.

3. Hardware implementation

In this section, the hardware implementation of the TFPA method is presented, including focusing and beamforming circuits and the overall architecture of the image formation logic.

3.1. Focusing circuit

Once the virtual array was obtained by (1) and (2) specialized digital circuits to perform dynamic focusing in real time in homogeneous media can be used. In general, published focusing circuits use few hardware resources and operate from an initial state defined by a set of values. For the circuit proposed in [24], only 3 values for registers (R, B and D) are needed to define the initial state. Then, during acquisition, the circuit yields a single-bit focusing code Q to indicate if the next sampling instant must advanced ($Q = 1$) or not ($Q = 0$), which keeps the timing errors below a predefined threshold [28]. These 3 values (R, B, D) are all the information required to provide properly delayed samples for coherent addition along the propagation path. They are obtained from the virtual array and the inspection parameters with closed formulae, which is a fast process. Every ultrasonic channel uses a focusing circuit for each scan line and a set of $N{\cdot}L$ focusing circuits is required for an image with L lines. The volume of information for beamforming is just $3{\cdot}N{\cdot}L$ values, which contrasts with the considerably higher requirement of TFM, where O·N·L delays are needed, being O the number of pixels per line (usually $\mathrm{O} \gg 3$). For example, for $\mathrm{L} = 200$, $\mathrm{O} = 200$ and $\mathrm{N} = 64$, in TFM, a total of $200{\cdot}200{\cdot}64 \approx 2.5$ M values must be computed. In TFPA the number of parameters to build the image is $3{\cdot}64{\cdot}200 \approx 40$ K, a difference of several orders of magnitude.

Furthermore, the proposed approach makes unnecessary the computation of TOFs to image pixels or the storage of indexes for beamforming, with propagation in single or dual media. In fact, the focusing hardware produces focused samples from all channels at the same rate the wavefront propagates along the scan line (strict real time).

3.2. Beamforming

Following the omnidirectional emission from a single element or virtual source, all elements are used in reception to get N A-scans. Due to the unfocused emission a low-resolution image is obtained. The sequence is repeated changing the emitter position until all array elements have been used as emitters, which produces N low-resolution images. The final high-resolution image is obtained as the average of the N precedent images.

After emission with element i, the echoes recorded by the N ultrasonic channels are used to build the image I_i. Beamforming is carried out by the focusing circuit on samples located over the image scan lines at intervals $\Delta R = c_2 T_S/2$. The combination of the results of two focusing circuits, one for the emitter and the other for every receiver, both acting on the same scan line, performs DDFF in real time. The emitter circuit provides the code bit Q_E that, combined with the code bits Q_R of the N receiving elements, forms a set of 2-bit emission and reception focusing code. The resulting two-bit focusing code informs every channel of the beamformer to get the next sample after 1, $1\text{–}1/\nu$ or $1\text{–}2/\nu$ sampling

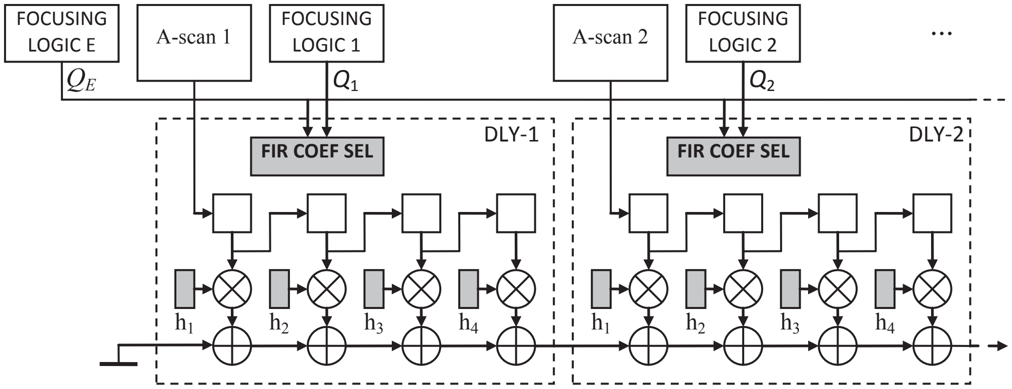

Fig. 6. The TFPA beamformer architecture based on DSP cells available in FPGAs.

periods, with *v* a design parameter that determines the delay resolution. This adjusts the sampling instants to produce coherent data in all the channels simultaneously, which can be added together to obtain the output sample.

Ideally, the *v* parameter should be high enough to avoid the presence of quantization lobes, being generally accepted that the delay resolution should be kept below 1/32–1/16 of the signal fundamental period [27]. For example, a 64 elements and 5 MHz array sampled at 40 MSPS, would require $v = 4$ to achieve a delay resolution of 1/32 of the fundamental period. On the other hand, it should be kept as low as possible to reduce the hardware complexity.

Fig. 6 shows the TFPA beamformer architecture, which implements the delay-and-sum function as a FIR filter with the DSP cells available in state-of-the-art FPGAs. It is a distributed architecture, modular and scalable to any number of ultrasound channels (only two are shown). Channel *i* has a delay module DLY-*i* based on a fractional filter FIR structure that provides the interpolated samples for coherent addition, performed in pipeline with results of other channels.

The process produces a single DDFF scan line in real time. However, current FPGA technology allows obtaining multiple DDFF scan lines in parallel, reusing hardware to perform several delay-and-sum operations every sampling period. If f_C is the DSP cell maximum switching rate and f_S is the sampling frequency, the hardware reuse ratio *r* theoretically can reach up to f_C/f_S meaning that *r* scan lines could be simultaneously processed, sharing the same hardware and changing only data and coefficients.

Although state-of-the-art FPGAs allow f_C rates above 700 MHz [29] other FPGA fabric components are unable to reach even half of that frequency, moreover when FPGA resources are near completely used. Then, in our prototype we used a conservative figure $f_C = 200$ MHz that allows processing $A = 4$ scan lines simultaneously for a sampling rate $f_S = 50$ MHz. Such figure would be even higher for lower sampling rates, increased f_C or higher performance FPGAs. Furthermore, current technology allows integrating several multi-line beamformers in a device. We implemented $B = 8$ multi-line beamformers for $C = 32$ channels in a moderately sized XC7K325T-2 Kintex FPGA. It produces $K = A{\cdot}B = 32$ beamformed lines in parallel at $f_S = 50$ MHz, a figure that would double if the sampling frequency were halved.

3.3. Real-time imaging

Ideally, the *L* lines that compose an image should be beamformed in parallel with the data acquisition process. However, as it has been pointed out, such strict real-time possibility depends on the sampling frequency and FPGA size and performance. Currently this could be achieved with higher-end FPGAs (for instance, the UltraScale devices from Xilinx [30]).

If resources are limited, a single FPGA acquires data from $C < N$ channels and beamforms $K < L$ scan lines in parallel. Increasing the number of FPGAs overcomes the first limitation. For example, if $N = 128$ and $C = 32$, 4 FPGA modules are required as in our current TFPA prototype without any other change. The proposed beamforming architecture does not introduce timing penalties other than latency.

A different problem appears when $K < L$ due to hardware resource limitations. In this case, the solution is beamforming the image in blocks of *K* lines each time. Obtaining the whole image requires repeating the multi-line beamforming process $[L/K]_\uparrow$ times, where $[\cdot]_\uparrow$ is rounding up. Each time the original acquired data is reused and the set of focusing parameters $\{R, B, D\}$ is changed. Although not strictly in real time, images can anyway be obtained at a high rate.

For example, a $\theta_S = 90^\circ$ sector image at $\Delta\theta = 1/N$ intervals, acquired with a $d = \lambda/2$, $N = 128$ element array, produces $L = 201$ scan lines. If $K = 32$, at least 7 multi-line beamforming cycles are required. For a 100 mm thick, $c_2 = 6$ mm/µs part, the acquisition time is 33.3 µs. Image beamforming requires the time of 7 acquisitions, or 233 µs. This yields an image rate capability of over 33 images/s with DDFF.

4. Experimental verification

To verify the operation of the proposed TFPA technique, as well as to assess the influence of the TOF errors associated to the virtual array, a set of experiments were carried out. They were performed with a 5 MHz, 128-element, 0.65 mm pitch array (Imasonic, France) and signals acquired with a SITAU-111 full parallel, 128-channels phased array system (Dasel, Spain), with $v = 4$ in all cases.

The main objective is to compare the images obtained with PA, TFM and TFPA techniques. To this purpose, complete data sets were acquired (FMC) by scanning a single-element emitter through the whole array and receiving and storing *N* A-scans in parallel following every trigger event. This yields the FMC with N^2 A-scans, which were used to build images with the three techniques (PA, TFM and TFPA).

4.1. Experiment 1. Resolution and dynamic range of PA, TFM and TFPA

An experiment was performed on an aluminum block with pairs of 1.5 mm diameter holes (SDHs) separated 3 mm in the lateral direction and 10 mm in depth. The array was placed approximately parallel to the interface at a distance of 30 mm, with its centre at x = 40 mm in water immersion and sector images were built with PA (Fig. 7a and b), TFM (Fig. 7c) and TFPA (7d), in linear scale and normalized to the maximum value. Imaging range is 10–70 mm from the interface, and scanning angles from −40° to 40°.

The emission focus for PA was set at midrange from the interface (35 mm), with apertures of 128 elements (Fig. 7a) and 24 elements (Fig. 7b). DDF was used in reception in both cases and the virtual array technique was applied, setting the reference foci F_A and F_B at ranges $R_A = 16$ mm and $R_B = 46$ mm, respectively.

Resolution of the third SDH pair in Fig. 7a is equivalent to that of

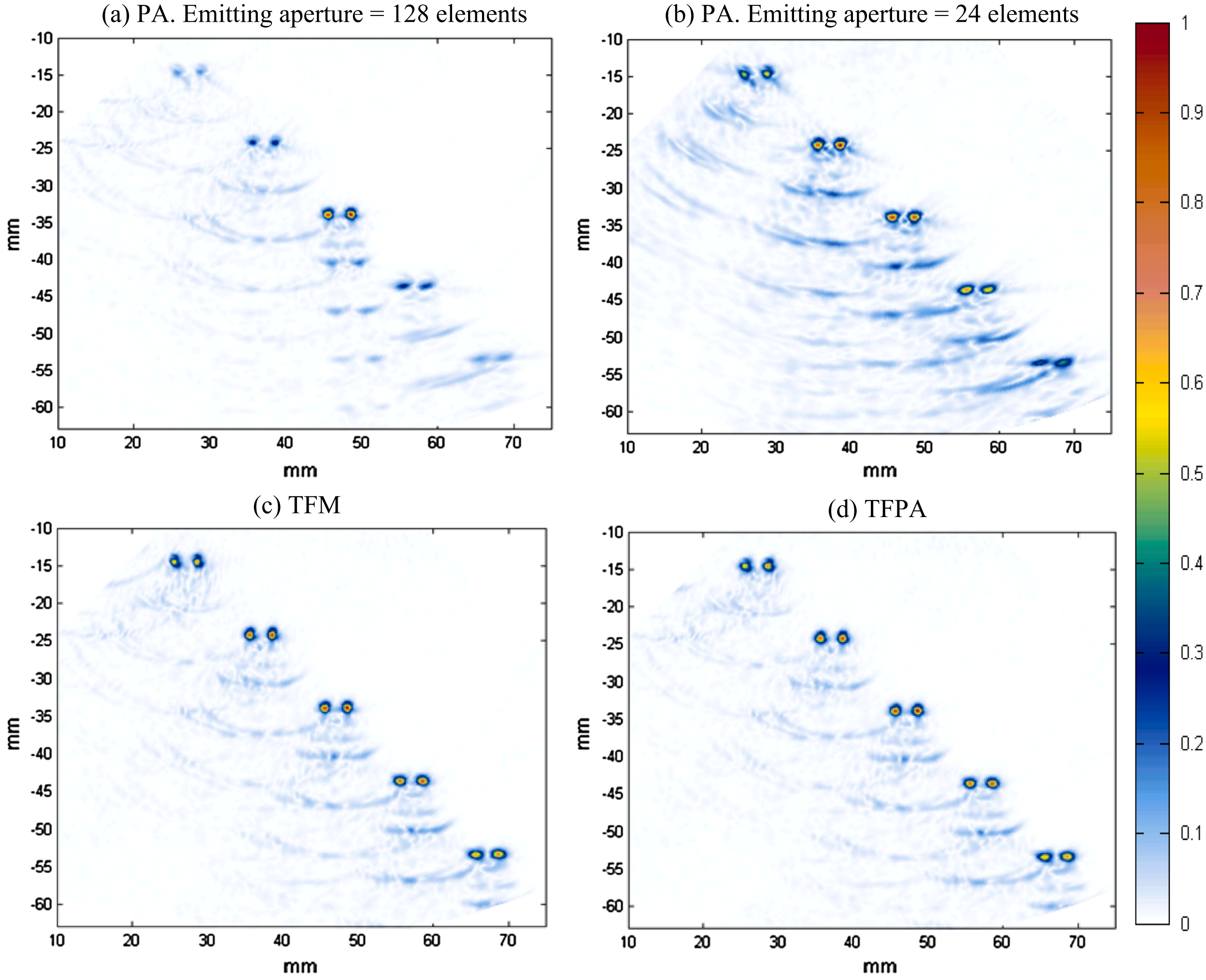
(a) PA. Emitting aperture = 128 elements

(b) PA. Emitting aperture = 24 elements

(c) TFM

(d) TFPA

Fig. 7. Resolution experiment: (a) Set up, (b) PA using Virtual Array, (c) TFM and (d) TFPA.

TFM, since its depth coincides with the PA emission focus and DDF is used in reception. At other ranges resolution worsens and the indications amplitude is reduced because the short focal depth.

The image in Fig. 7b was acquired with a larger focal depth (50 mm), showing improved amplitude homogeneity, but slightly lower lateral resolution. Furthermore, since the emitted energy is lower, the relative amplitude of the reverberation and mode converted signals in the region below the SDHs increases, approaching that of some true indications.

In contrast, Fig. 7c shows the TFM image, where all pixels are focused in emission and in reception. TOFs were calculated with an iterative Fermat procedure that yield timing errors below 1 ns. These TOFs can be assumed exact, although obtained with a considerable computing effort. Resolution is very good, amplitude variations with depth are small and acoustic noise is limited.

Fig. 7d shows the TFPA image obtained with the virtual array and the same settings than for PA (F_A at 16 mm and F_B at 46 mm). The computing effort to get the virtual arrays was orders of magnitude lower than computing the TOFs by Fermat. The virtual array timing errors were of the order of those analyzed in precedent sections. When comparing this image with that of TFM in Fig. 7c it is really difficult to find essential differences. In both cases, resolution is fairly good, acoustic noise is lower than in the PA image and echo amplitudes are rather uniform in the whole range.

Fig. 8 shows the lateral pattern obtained as the normalized amplitude in dB along every scan line with the three imaging modalities of Fig. 7b–d. In general TFM yields slightly better resolution, but it is practically indistinguishable from that provided by TFPA. Amplitude is also quite similar in TFM and TFPA, differing in less than 1 dB in the whole range. Resolution and sidelobe levels of PA are worse because fewer elements are used in emission and, sometimes, the amplitude of the indications falls by up to 4 dB with regard to that of TFM and TFPA.

Table 1 shows the Full Width Half Maximum (FWHM) of the 10 SDHs with $N = 128$. The best resolution of PA is achieved slightly before the emission focus at the second pair of SDHs, at 24 mm. TFM resolution is better than that of TFPA for all SDHs although by a small difference: TFPA resolution is about a 20% lower than that of TFM at the smaller range (14 mm), where some extreme elements do not participate in the image beamforming (dynamic aperture). At other ranges, TFPA resolution is quite similar to that of TFM, with much lower variations. Maximum virtual array timing errors of 16 ± 12 ns are found at 24 mm, in agreement with those numerically computed, although they do not affect resolution in practice.

4.2. *Experiment 2. Imaging near the interface*

In general, the Virtual Array shows increased timing errors on locations very close to the interface, as presented in Section 2. However TFPA operates with dynamic aperture by blocking the participation of extreme elements in the beamforming process, reducing the timing errors as discussed in Section 2.

Therefore, it can be expected that imaging near the interface with TFPA provides lower resolution than that obtained with TFM because of dynamic aperture. On the other hand, depending on the relative

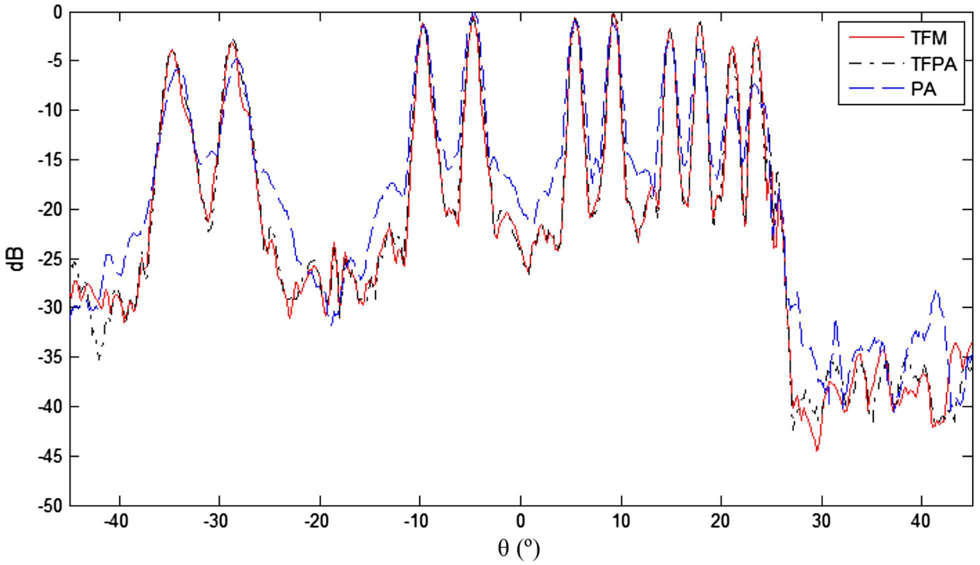

Fig. 8. Normalized lateral pattern of PA, TFM and TFPA as a function of steering angle θ (dB).

distance of the array to the interface and aperture size, the influence of the extreme elements in the near field is low due to angular sensitivity loses, an effect that is common to all imaging modalities.

Fig. 9a shows a SDH of 1 mm diameter located at 1.2 mm from the surface of an aluminum part in immersion, with the same array used in the precedent cases. Fig. 9b–d show a detail of the normalized images obtained with different methods and parameters, with axes in mm and coordinates origin at the array element 1.

Fig. 9b is the TFM image of the SDH, clearly visible with excellent resolution. Fig. 9c shows the TFPA image with foci F_A and F_B placed at 16 and 46 mm from the interface, respectively, as in precedent cases. The resolution gets worse, the indication has been shifted laterally by about 0.5 mm and the sidelobe level increases, effects that can be attributable to the virtual array timing errors and the dynamic aperture.

Fig. 9c shows the TFPA image when F_A and F_B are placed at 3 and 18 mm from the interface, respectively. Here resolution and position of the echo maximum are recovered and the sidelobe level again becomes low. This image is quite similar to that of TFM with a slight resolution loss due to the dynamic aperture effect.

Thus, for highly accurate imaging near the interface, it is advisable to set the reference foci at shorter ranges in TFPA. For general purpose imaging, they can be arbitrarily set at about 10% and 60% of the full range. Two different settings could give high quality images at near and far ranges, without requiring new data acquisitions.

4.3. Experiment 3. Imaging a curved part

A final experiment was carried out to test the validity of TFPA for imaging a curved interface aluminum part in immersion (Fig. 10a). Since the relative positions of the array probe with the part were unknown, the geometry was estimated following the pulse-echo auto-focusing procedure described in [25]. Points at the interface were detected and fitted to a circle, which provided an analytical representation of the interface geometry to compute TOFs by Fermat (TFM) or by the Virtual Array (PA and TFPA).

Fig. 10b shows the PA image obtained with DDF in reception and a 128-element emitting aperture with the focus set at mid-range (35 mm). This setting provides better resolution for the group of SDHs nearest to the interface, where SDH (c) is at the focal depth. By contrast, the amplitude of the SDH (a) in this group is lower due to the shadowing effect of the other holes.

Fig. 10c shows the TFM image obtained with the full aperture. As in the precedent cases, it provides an excellent resolution, uniform amplitude and low noise in the whole image range. The TFPA technique was applied to the detected interface, computing the virtual array with F_A and F_B set at 10% and 60% of the 70 mm image range. The 128-elements of the 5-MHz array probe were used, which produced the image shown in Fig. 10d. An excellent agreement with the TFM image is obtained, with both images being practically indistinguishable with regard to resolution and noise.

Table 2 yields the measured FWHM of the 8 SDHs for the three imaging modalities, with a mean of 1.55 mm for PA, 1.04 mm for TFM and 1.12 mm for TFPA. In practice, the resolution of TFM and TFPA are similar and nearly a 50% better than that of PA due to focusing in emission and in reception. Timing errors for this configuration by the application of the Virtual Array concept remain basically below 20 ns, 10 times lower than the signal period. This results in low focusing errors with regard to the exact TOF calculations using iterative techniques and the Fermat's principle.

5. Conclusions

A new delay-and-sum beamforming technique, the Total Focusing Phased Array (TFPA) has been proposed, analyzed and experimentally verified. TFPA beamforming is carried out along straight paths, as in Phased Array (PA), but with emission and reception focusing, as in the

Table 1
FWHM and timing error statistics for the 5 SDHs pairs of Fig. 7, $N = 128$.

Depth (mm)	−14	−14	−24	−24	−33	−33	−43	−43	−53	−53	Mean	STD
FWHM PA (mm)	1.35	1.17	1.17	1.11	1.31	1.30	1.67	1.63	2.38	2.70	1.35	1.63
FWHM TFM (mm)	0.96	0.82	0.85	0.79	0.92	0.89	1.13	1.10	1.40	1.38	0.96	0.67
FWHM TFPA (mm)	1.16	1.05	0.96	0.92	0.98	0.94	1.14	1.11	1.42	1.40	1.16	0.54
Timing mean error (ns)	3.0	1.7	16.6	16.3	12.4	11.5	1.0	0.3	−9.86	−10.84	–	–
Timing STD error (ns)	4.4	4.3	11.2	12.0	8.7	9.8	5.1	4.7	8.17	9.72	–	–

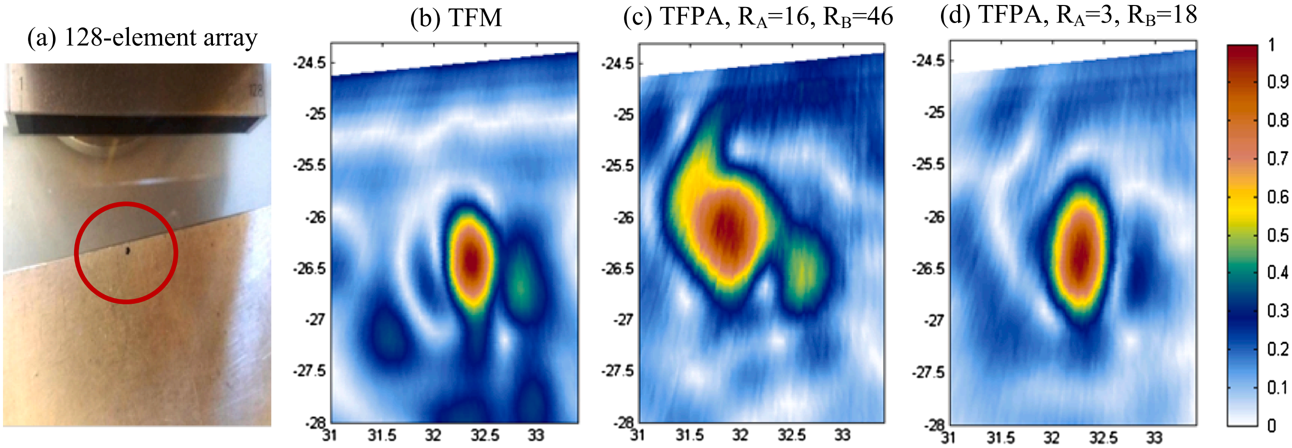

Fig. 9. (a) Acquisition set up, (b) TFM image, (c) TFPA image with $R_A = 16$ mm, $R_B = 46$ mm, (d) TFPA image with $R_A = 3$ mm, $R_B = 18$ mm. Axes in mm.

Total Focusing Method (TFM). This is achieved by circuits that continuously adjust the delay applied to samples for coherent addition.

Beamforming along propagation paths allows an efficient hardware implementation that performs in real-time and has very moderate resource requirements. Furthermore, TFPA preserves the A-scan information. Application of the Virtual Array (VA) concept, allows TFPA to avoid refraction issues when crossing an interface between two propagation media.

The performance of TFPA, PA and TFM has been experimentally compared. The proposed real-time beamforming circuits guarantee timing errors below T_S/v, where T_S is the sampling period and $v > 1$, the equivalent oversampling factor. These are the maximum timing

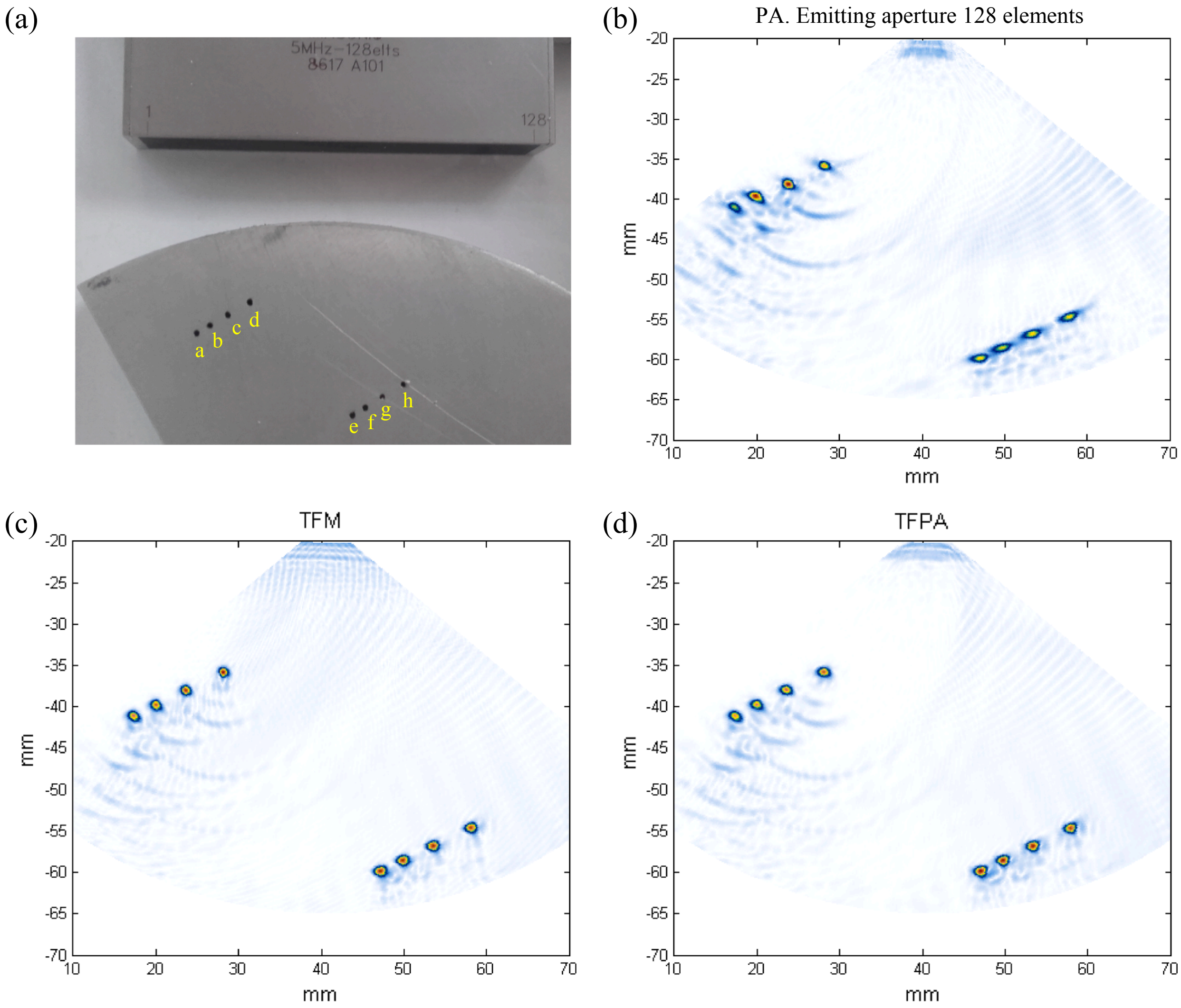

Fig. 10. (a) Inspection of a curved part in water immersion with interface auto-detection; (b) PA image with 128 emitting elements; (c) TFM image; (d) TFPA image.

Table 2
FWHM and timing error statistics for the 8 SDHs in Fig. 10, $N = 128$.

	a	b	c	d	e	f	g	h	Mean	STD
FWHM PA 128 EMI (mm)	1.44	1.36	1.04	1.18	1.75	1.98	1.80	1.86	1.55	0.91
FWHM TFM (mm)	1.13	1.03	0.91	0.81	1.17	1.12	1.12	1.06	1.04	0.33
FWHM TFPA (mm)	1.20	1.13	1.05	1.07	1.13	1.13	1.14	1.10	1.12	0.12
Timing mean error (ns)	9.7	13.8	16.7	18.3	−20.8	−18.2	−14.5	−14.0	–	–
Timing STD error (ns)	11.6	14.8	15.6	15.5	12.4	10.7	10.9	11.0	–	–

errors produced with TFPA when inspecting a homogeneous medium with strict focusing in emission and in reception.

With two propagation media the VA concept provides an approximate solution that converts the refraction problem into a homogeneous case. Here focusing is achieved with small timing errors that produce subtle amplitude losses and a slight increase on the sidelobe levels with regard to TFM. However, it has been experimentally shown that these effects can be neglected in practice and, in general, the advantages of TFPA outweigh their marginal shortcomings.

Acknowledgement

Dr. Jorge Fernández received fellowship PTQ-17-09089 of the 'Programa Torres Quevedo' of the Spanish Ministry of Economy and Competitiveness. This work is partially supported by the project RTI2018-099118-A-I00 founded by MCIU/AEI/FEDER, UE.

References

[1] M. Karaman, P.C. Li, M. O'Donnell, Synthetic aperture imaging for small scale systems, IEEE Trans. Ultrason. Ferroelec. Freq. Contr. 42 (1995) 429–442.
[2] G.R. Lockwood, F.S. Foster, Design of sparse array imaging systems, Proc. IEEE Ultrasonic Symp. 1995, pp. 1237–1243.
[3] P.D. Corl, P.M. Grant, G.S. Kino, A digital synthetic focus acoustic imaging system for NDE, Proc. IEEE Ultrasonic Symp. 1978, pp. 263–268.
[4] G.S. Kino, D. Corl, S. Bennett, K. Peterson, Real time synthetic aperture imaging system, Proc. IEEE Ultrasonic Symp. 1980, pp. 722–731.
[5] R.Y. Chiao, L.J. Thomas, S.D. Silverstein, Sparse array imaging with spatially-encoded transmits, Proc. IEEE Ultrasonic Symp. 1997, pp. 1679–1682.
[6] K.L. Gammelmark, J.A. Jensen, Multielement synthetic transmit aperture imaging using temporal encoding, IEEE Trans. Med. Imag. 22 (2003) 552–563.
[7] C. Holmes, B. Drinkwater, P. Wilcox, Post-processing of the full matrix of ultrasonic transmit–receive array data for non-destructive evaluation, NDT & E Int. 38 (8) (2005) 701–711.
[8] L. Bernus, A. Bulavinov, D. Joneit, M. Kröning, M. Dalichov, K. M. Reddy, Sampling phased Array a new technique for signal processing and ultrasonic imaging, ECNDT 2006, We.3.1.2, Berlin, 25–29 Sept., 2006.
[9] P.D. Wilcox, C. Holmes, B.W. Drinkwater, Advanced reflector characterization with ultrasonic phased arrays in NDE applications, IEEE Trans. Ultrason. Ferroelectr. Freq. Control 54 (8) (2007) 1541–1550.
[10] A.J. Hunter, B.W. Drinkwater, P.D. Wilcox, The wavenumber algorithm for full-matrix imaging using an ultrasonic array, IEEE Trans. Ultrason. Ferroelec. Freq. Contr. 55 (2008) 2450–2462.
[11] C. Holmes, B.W. Drinkwater, P.D. Wilcox, Advanced post-processing for scanned ultrasonic phased arrays: application to defect detection and classification in non-destructive evaluation, Ultrasonics 48 (2008) 636–642.
[12] J. Zhang, B.W. Drinkwater, P.D. Wilcox, A.J. Hunter, Defect detection using ultrasonic arrays: the multi-mode total focusing method, NDT & E Int. 43 (2) (2010) 123–133.
[13] A. Hunter, B.W. Drinkwater, P.D. Wilcox, The wavenumber algorithm for full-matrix imaging using an ultrasonic array, IEEE Trans. Ultrason. Ferroelectr. Freq. Control 55 (11) (2008) 2450–2462.
[14] J. Lambert, A. Pédron, G. Gens, F. Bimbard, L. Lacassagne, E. Iakovleva, Analysis of multicore CPU and GPU toward parallelization of total focusing method ultrasound reconstruction, in: DASIP 2012 Conf. on Design and Architectures for Signal and Image Processing, Karlsruhe, Germany, Oct 2012.
[15] M. Njiki, S. Bouaziz, A. Elouardi, O. Casula, O. Roy, A Multi-FPGA implementation of real-time reconstruction using total focusing method, in: Proc. 2013 IEEE Int'l Conf. on Cyber Technology in Automation, Control and Intelligent systems, pp. 468-473, May 26–29, Nanjing, China, 2013.
[16] T.K. Song, S.B. Park, A new digital phased array system for dynamic focusing and steering with reduced sampling rate, Ultrasonic Imag. 12 (1990) 1–16.
[17] M. Karaman, A. Atalar, H. Köymen, VLSI circuits for adaptive digital beamforming in ultrasound imaging, IEEE Trans. on Med. Imag. 12 (4) (1993) 711–720.
[18] K. Jeon, M.H. Bae, S.B. Park, S.D. Kim, An efficient real time focusing delay calculation in ultrasonic imaging systems, Ultrasonic Imag. 16 (1994) 231–248.
[19] H.T. Feldkämper, R. Schwann, V. Gierenz, T.G. Noll, Low power delay calculation for digital beamforming in handheld ultrasound systems, Proc. IEEE Ultrason. Symp. 2 2000, pp. 1763–1766.
[20] R. Long, J. Rusell, P. Cawley, N. Habgood, Ultrasonic phased array inspection of flaws on weld fusion faces using full matrix capture, Rev. Prog. QNDE 28 (2009) 848–855.
[21] M. Parrilla, J. Brizuela, J. Camacho, A. Ibáñez, P. Nevado, C. Fritsch, Dynamic focusing through arbitrary geometry interfaces, IEEE Ultrasonics Symp. 2008, pp. 1195–1198.
[22] L. Le Jeune, S. Robert, P. Dumas, A. Membre, C. Prada, Adaptive ultrasonic imaging with the total focusing method for inspection of complex components immersed in water, in: Rev. Progress QNDE, 34, AIP Conf. Proc. 1650, 1037, Boise, Idaho, 2015.
[23] M. Suttcliffe, M. Weston, B. Dutton, I. Cooper, Real-time full matrix capture with auto-focusing of known geometry through dual layered media, in: NDT Conf. of BINDT, Daventry, UK, 11–13 Sept. 2012.
[24] J.F. Cruza, J. Camacho, L. Serrano, C. Fritsch, New method for real-time dynamic focusing through interfaces, IEEE Trans. Ultrason. Ferroelectr. Freq. Control 60 (4) (2013) 739–751.
[25] J. Camacho, J.F. Cruza, J. Brizuela, C. Fritsch, Automatic dynamic depth focusing for NDT, IEEE Trans. Ultrason. Ferroelectr. Freq. Control 61 (4) (2014) 673–684.
[26] J.F. Cruza, J. Camacho, J.M. Moreno, C. Fritsch, Ultrafast hardware-based focal law calculator for automatic focusing, NDT&E Int. 74 (2015) 1–7.
[27] D.K. Peterson, G.S. Kino, Real-Time digital image reconstruction: a description of image hardware and an analysis of quantization errors, IEEE Trans. Sonics Ultrasonics 31 (4) (1984) 337–351.
[28] C. Fritsch, M. Parrilla, A. Ibáñez, R. Giacchetta, O. Martínez, The progressive focusing correction technique for ultrasound beamforming, IEEE Trans. Ultrason. Ferroelectr. Freq. Control 53 (10) (2006) 1820–1831.
[29] Xilinx, 7 Series FPGA data sheet: overview, DS-180, v 2.4, March 28, 2017.
[30] Xilinx, UltraScale architecture and product data sheet: overview, DS-890 (v.3.3), March 12, 2018.